

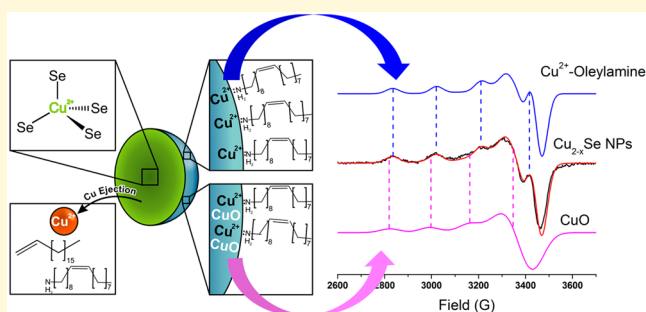
Evolution of Surface Copper(II) Environments in Cu_{2-x}Se Nanoparticles

Derrick C. Kaseman,[†] Austin Gamble Jarvi,[†] Xing Yee Gan,[†] Sunil Saxena,^{*,†,‡} and Jill E. Millstone^{*,†,‡,§}

[†]Department of Chemistry, [‡]Department of Chemical Engineering, and [§]Department of Mechanical Engineering and Materials Science, University of Pittsburgh, Pittsburgh, Pennsylvania 15260, United States

Supporting Information

ABSTRACT: Cu_{2-x}Se nanoparticles are part of a promising class of alternative plasmonic materials where the location, stability, and structural impact of charge carrier generation are crucial to their optoelectronic performance. Here, electron paramagnetic resonance spectroscopy is used to identify the location and dynamics of Cu^{2+} environments that form upon air-induced oxidation of Cu_{2-x}Se nanoparticles. The results indicate the formation of two distinct Cu^{2+} environments at or near the surface of the nanoparticle. The first environment can be assigned to Cu^{2+} bound to oleylamine capping ligands, and the second can be assigned to Cu^{2+} located in CuO domains. In addition, these experiments indicate that the observed Cu^{2+} environments are consistent with vacancy formation on the Cu sublattice, which are mobile (i.e., vacancy hopping) at temperatures down to 180 K. Taken together, our results elucidate time scales of air-mediated Cu oxidation in Cu_{2-x}Se nanoparticles, the chemical environments of the resulting Cu^{2+} species, and the impact of this oxidation on the overall particle crystallographic structure and optoelectronic properties.



INTRODUCTION

Nanoparticles (NPs) containing low valent metal atoms such as Cu, Fe, and Ni are widely studied materials with a variety of applications.^{1–5} An important subset of these applications relies on the oxidation of the metal atoms, the subsequent generation of free charge carriers, and ultimately the response of these carriers to incident radiation (e.g., localized surface plasmon resonances, LSPRs).^{5–7} Therefore, a fundamental understanding of the location and dynamics of these oxidation reactions is crucial to both obtain and tailor their optoelectronic properties.

In particular, copper chalcogenide NPs (Cu_{2-x}S ,^{8–11} Cu_{2-x}Se ,^{4,10,12} and Cu_{2-x}Te ¹³) display LSPRs in the mid- to near-infrared regions, making them attractive for photothermal therapy,^{8–11} sensing,^{9–11} and spectroscopy.¹³ The appearance of an LSPR in these materials depends on the oxidation of Cu^+ sites, which generates hole charge carriers.^{4,5,14} Several studies have shown that these LSPR features can then be tuned by controlling the extent of Cu oxidation.^{4,15–17}

However, there remains considerable ambiguity in the stoichiometry and chemical environments of Cu in copper chalcogenide NPs, and specifically the population and location of Cu^+ and Cu^{2+} species.^{15,16,18,19} Recent studies have begun to address this ambiguity. For example, in the synthesis of Cu_{2-x}Se NPs, Manna and co-workers have used transmission electron microscopy (TEM) and scanning TEM energy dispersive X-ray spectroscopy (STEM-EDS) to identify small

CuO NPs that form concomitantly as a function of time, during the oxidation of the original Cu_2Se NPs.¹⁵ The authors attribute the presence of these CuO NPs to Cu^{2+} leaving the original Cu_{2-x}Se NPs. The authors also observe a thin coating of oxygen on the Cu_{2-x}Se NPs themselves, consistent with an additional CuO layer present at the surface of the Cu_{2-x}Se NPs. Prieto et al. have also observed the presence of surface CuO on Cu_{2-x}Se NPs using a detailed analysis of X-ray photoelectron spectroscopy (XPS), powder X-ray diffraction (PXRD), and electrochemical measurements.¹⁹ The authors suggest that a diffusion gradient is established within the NP between Cu^+ and Cu^{2+} , which drives Cu^+ to the surface (i.e., vacancy formation) and results in x Cu deficiencies in the Cu_{2-x}Se core. Talapin, da Como, and co-workers also suggest that most Cu does not leave the particle upon oxidation, and instead that Cu^{2+} species are distributed throughout the particle with some coordinated to pendant ligands and some ions sequestered in surface CuO layers.¹⁶ Interestingly, recent work by Gamelin et al. has shown that the plasmonic features of Cu_{2-x}S NPs can arise both with or without the presence of cation vacancies, and the presence of these vacancies is dictated by the particle oxidation pathway.¹⁸

Received: September 18, 2018

Revised: September 25, 2018

Published: October 10, 2018

Taken together, these studies highlight important insights, as well as important unknowns, regarding the mechanism of copper chalcogenide NP oxidation, the chemical environment of the oxidized Cu^{2+} species, and the formation, dynamics, and fate of the resulting Cu^{2+} . The ability to detect, quantify, and structurally assign these metal centers is important in both the copper chalcogenides and, indeed, all classes of semiconductor NPs. This information not only allows one to control and interpret their optoelectronic features but also to direct their synthesis *de novo*, to control final particle architectures (especially surface structures), and ultimately to dictate their technological performance.

Here, we investigate the evolution of Cu^{2+} environments during Cu_{2-x}Se NP oxidation (specifically, oxidation via air exposure of a chloroform NP solution) using electron paramagnetic resonance (EPR) spectroscopy. EPR is uniquely suited to study the oxidation of Cu in these materials because only Cu^{2+} is detectable using this technique. Our results provide insight into the time scales of Cu^{2+} oxidation, identify Cu^{2+} chemical environments, and elucidate the impact of Cu oxidation on the structure and observed optoelectronic properties of the resulting Cu_{2-x}Se NPs.

■ EXPERIMENTAL SECTION

Materials and Methods. Copper(I) chloride (CuCl , >99.995%), copper(II) chloride (CuCl_2 , >99.99%), selenium powder (Se, >99.5%), octadecene (ODE, 90% technical grade), oleylamine (OLA, 70% technical grade), chloroform (>99%), chloroform-*d* (99.8%), copper(II) acetylacetonate (Cu-acac , >99.99%), bulk copper(I) selenide (Cu_2Se , >99.95%), and copper(II) oxide (CuO , >99.99%) were purchased from Sigma-Aldrich (St. Louis, MO). Absolute ethanol (EtOH) was purchased from Thermo Fisher Scientific (Pittsburgh, PA). All chemicals were used as received with no additional purification unless otherwise noted. Prior to use, all glassware and Teflon stir bars were washed in aqua regia and rinsed with copious amounts of water prior to oven drying. *Caution: aqua regia is highly toxic and corrosive and should only be used with proper personal protective equipment and training. Aqua regia should be handled only inside a fume hood.*

Synthesis of Cu_{2-x}Se NPs. Cu_{2-x}Se NPs were synthesized using a previously described hot injection method.^{4,20} The synthetic procedure was completed using standard air-free techniques and is described in detail below. The selenium–octadecene–oleylamine mixture was created by dissolving 80 mg of Se in 1 mL of ODE and 2 mL of OLA. The solution was heated in a round-bottom flask for 12 h under argon gas at 195 °C. In a three-neck round-bottom flask, 200 mg of CuCl was added with 5 mL of OLA and 5 mL of ODE. The Cu –ODE–OLA mixture was heated to 140 °C under vacuum for 30 min and then heated to 285 °C under Ar. Then, the Se mixture was injected into the Cu mixture. The precursors reacted for 10 min at ~285 °C to form Cu_{2-x}Se NPs. The NPs were cooled to room temperature by removing the heating mantle.

NPs were purified by centrifugation to remove unreacted precursors, reaction byproducts, and excess ligands. For purification, 6.5 mL aliquots of as-synthesized particle mixture were separated and transferred to centrifuge tubes; 10 mL of EtOH was then added to each tube and centrifuged in an Eppendorf 5804R centrifuge at 2850 rcf for 10 min. The supernatant was discarded, and the precipitate was resuspended with chloroform and sonicated. To this suspension, 10 mL of EtOH was added, and the centrifugation procedure was repeated. The purified particles were characterized using TEM, extinction spectroscopy, EPR, PXRD, XPS, and nuclear magnetic resonance (NMR) spectroscopy.

Synthesis of Cu@CuO NPs. Cu@CuO NPs were synthesized using a modified procedure by Yang et al.²¹ In this synthesis, 105 mg of Cu-acac was added to 10 mL of OLA in a 25 mL three-neck round-bottom flask on a magnetic stir plate. The solution was placed under

Ar and degassed three times for 5 min each. The mixture was slowly heated to 230 °C and kept at 230 °C for 6 h before cooling to room temperature. The particles were washed three times using a chloroform–ethanol (1:10) mixture and centrifugation at 2850 rcf for 10 min.

EPR Cu_{2-x}Se NP Oxidation Study. The oxidation process of the NPs was performed by transferring the washed NPs suspended in 150 μL of chloroform to a 4 mm quartz EPR tube. The aging study was performed by blowing house air into an EPR tube via a needle at a pressure that created turbulence on the surface of the solution. Before each EPR measurement, the particles were diluted to 150 μL with chloroform to account for any solvent evaporation and sonicated for 10 min before flash freezing in liquid N_2 .

EPR Measurements. Continuous wave (CW) EPR measurements were performed on a Bruker ElexSys E580 FT/CW X-band spectrometer using a Bruker ER4118X-MD5 resonator at 80 K. All CW experiments were run with a center field of 3100 G and a sweep width of 2000 G, modulation amplitude of 4 G, and a modulation frequency of 100 kHz for 1024 data points using a conversion time of 20.48 ms. All EPR simulations were performed using EasySpin software.²²

Three-pulse electron-spin echo envelope modulation (ESEEM) experiments were performed on a Bruker ElexSys E580 X-band FT/CW spectrometer equipped with a Bruker ER4118X-MD5 resonator. The temperature for all experiments was controlled using an Oxford ITC503 temperature controller with an Oxford ER 4118CF gas flow cryostat. Experiments were performed at X-band frequencies at 80 K. A $\pi/2$ – τ – $\pi/2$ – T – $\pi/2$ –echo pulse sequence was used. The $\pi/2$ pulse length was 16 ns, the initial time delay, τ , was 144 ns, and the second time, T , was initially set to 288 ns and incremented by 16 ns. A four-step phase cycling was used to eliminate unwanted echoes.^{23,24} ESEEM data were phase corrected, baseline subtracted, and Fourier transformed using Bruker WinEPR software.

Extinction Spectroscopy. Extinction spectroscopy measurements were performed on a Cary 5000 spectrophotometer (Agilent, Inc.) using 1 cm path length quartz cuvettes. Purified Cu_{2-x}Se NPs were suspended in 1 mL of chloroform and placed in the cuvettes. The spectra were recorded from 2000 to 350 nm at a rate of 1000 nm/min, with a source and detector changeover occurring at 850 nm. Spectra were baseline corrected with respect to 1 mL of neat chloroform.

Transmission Electron Microscopy (TEM). Samples were prepared for TEM by drop-casting 6 μL of the NPs (optical density (O. D.) = 1) on a carbon-coated Cu 200 mesh grid (Ted Pella, Inc.). TEM characterization was performed using a Hitachi H-9500 TEM with an accelerating voltage of 300 keV. The size distribution of the NPs was determined using >200 NPs from various positions on the grids and using ImageJ software (National Institutes of Health, USA).

X-ray Photoelectron Spectroscopy (XPS). XPS spectra were obtained using an ESCALAB 250XI XPS with a monochromated, microfocused Al $K\alpha$ X-ray source (spot size = 600 μm). Survey and high-resolution spectra were collected with a pass energy of 150 and 50 eV and a step size of 1.0 and 0.1 eV, respectively. Spectra were charge referenced to adventitious carbon (284.8 eV). NPs were drop-cast onto p-doped (boron) silicon wafers (University Wafer, Boston, MA) that had been cleaned for ultrahigh vacuum analysis.

XPS Cu_{2-x}Se NP Oxidation Study. The oxidation process of the NPs was monitored by drop-casting the washed NPs suspended in chloroform on a silicon wafer (*vide supra*). The wafer containing the NP sample was left in ambient conditions to further oxidize. The Cu 2p scan of the NP sample was monitored over the course of the next 230 h.

Powder X-ray Diffraction (PXRD). Cu_{2-x}Se NPs were characterized by PXRD using a Bruker AXS D8 Discover XRD (NanoScale Fabrication and Characterization Facility, Petersen Institute of NanoScience and Engineering, Pittsburgh, PA) at 40 kV and 40 mA for Cu $K\alpha$ ($\lambda = 1.5406 \text{ \AA}$) X-ray source with a scan speed of 0.8 s/step from 10.00° to 90.00° with a step size of 0.02°. Samples were prepared by drop-casting an aliquot of purified NP solution dispersed in chloroform on a glass microscope slide (Fisher

Scientific). The as-prepared Cu_{2-x}Se NP sample on the glass slide was left to oxidize in air over the course of several weeks and recharacterized. Bulk Cu_2Se and Cu_{2-x}Se powders were packed in 0.50 mm capillary tubes (Hampton Research) and flame-sealed for PXRD characterization. The PXRD pattern of these samples was collected using a Bruker X9 Prospector Ultra (Department of Chemistry, University of Pittsburgh) at 45 kV and 0.65 mA equipped with a $1\mu\text{S}$ microfocus $\text{Cu K}\alpha$ ($\lambda = 1.54178 \text{ \AA}$) X-ray source with a scan speed of 0.5 s/step from 12.00° to 108.00° with a step size of 0.02° .

Solid State NMR Spectroscopy. Solid state NMR measurements were performed on a Bruker 500 AVANCE spectrometer operating at 11.74 T ($^{77}\text{Se} = 95.35 \text{ MHz}$). Static NMR spectra were acquired using a $\pi/2$ ($2.83 \mu\text{s}$)– τ ($30 \mu\text{s}$)– π ($5.75 \mu\text{s}$)–acquire Hahn echo sequence. A 100 ms recycle delay was used for all experiments with ~ 20480 free induction decays (FIDs) collected and averaged per experiment. T_1 experiments were performed using an inversion recovery (π – τ – $\pi/2$ – $30 \mu\text{s}$ – π –acquire) method with π pulses replaced with composite pulses. Temperatures were externally calibrated using neat methanol, and all spectra were referenced to ammonium selenate ($\delta_{\text{iso}} = 1040.2 \text{ ppm}$).^{25,26}

^1H NMR Spectroscopy. All ^1H NMR measurements were performed on a Bruker 400 Ultrashield magnet with an AVANCE III 400 Console or a Bruker 600 Ultrashield magnet with an AVANCE III 600 Console (Bruker Biospin, Billerica, MA) at 298 K. For all experiments, a minimum recycle delay of 15 s was used, which was sufficiently greater than T_1 . NMR samples were prepared as described above by dissolving OLA, ODE, and EtOH in deuterated chloroform and by concentrating the Cu_{2-x}Se NPs in deuterated chloroform.

RESULTS

A representative CW EPR spectrum of the partially oxidized Cu_{2-x}Se NPs and the corresponding spectral simulation are shown in Figure 1. The spectrum was best fit using two

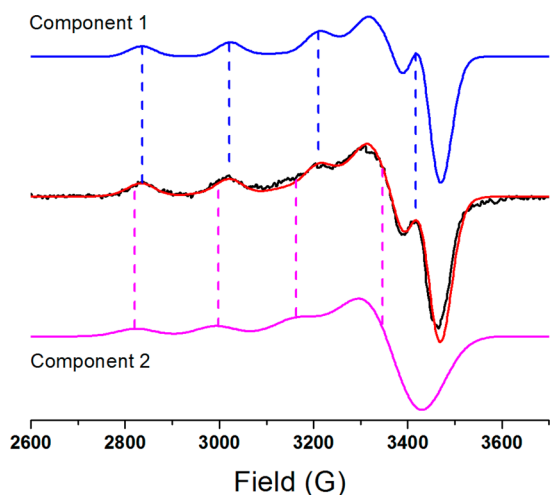


Figure 1. Representative simulation (red) of CW EPR spectrum obtained for Cu_{2-x}Se NPs after 43 h of oxidation (black). The multicomponent simulation (red) is a summation of component 1 (blue) and component 2 (pink). The A_{\parallel} splittings of each component are denoted by the blue and pink dashed lines.

components, and these are shown in blue and pink. Each component is characterized by two second rank tensors, the \mathbf{g} tensor (\mathbf{g}) and the hyperfine (\mathbf{hf}) tensor. The \mathbf{g} tensor is indicative of electronic environments of the unpaired electron, while the \mathbf{hf} tensor is related to electron–nuclear interactions. These tensors are diagonalized in their principal axis systems resulting in three principal components: g_{xx} , g_{yy} , and g_{zz} and

A_{xx} , A_{yy} , and A_{zz} . The measured spectra were consistent with axially symmetric \mathbf{g} and \mathbf{hf} tensors, in which $g_{xx} = g_{yy} \equiv g_{\perp}$, $g_{zz} \equiv g_{\parallel}$, $A_{xx} = A_{yy} \equiv A_{\perp}$, and $A_{zz} \equiv A_{\parallel}$.^{27,28} The splittings due to A_{\parallel} are more pronounced as shown by dashed lines in Figure 1. The presence of a second component indicates more than one electronic environment.

The evolution of the EPR spectra as a function of oxidation was monitored from 0 to 230 h (Figure 2 and Figure S1). The

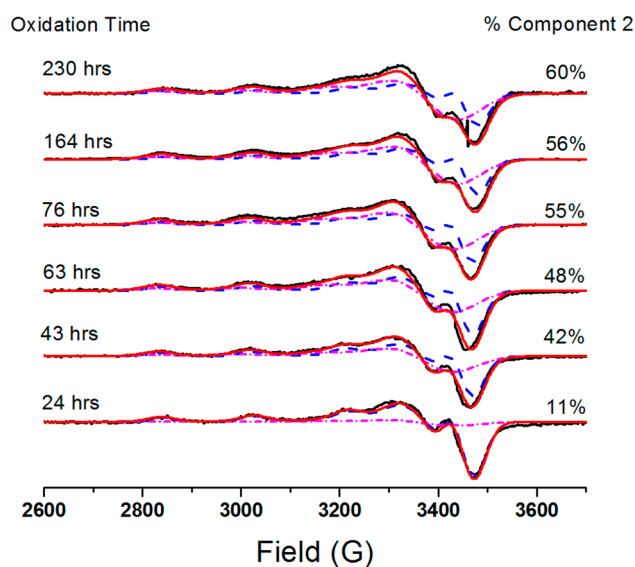


Figure 2. Experimental CW EPR spectra (solid black) and corresponding 2 component simulations (solid red) of Cu_{2-x}Se NPs as a function of oxidation. The simulated spectra of component 1 and component 2 are shown by a blue dashed line and a pink dot-dashed line, respectively. The total oxidation time is denoted to the left of each spectrum. The percentage of component 2 in each simulation (relative to component 1) is listed to the right of each spectrum.

Table 1. Best Fit Parameters for EPR Simulations of Cu_{2-x}Se NPs

	component 1	component 2
g_{\perp}	2.0468	2.0577
g_{\parallel}	2.2182	2.2475
A_{\perp} (G)	22	18
A_{\parallel} (G)	204	184
LB_{\perp} (G)	62	127
LB_{\parallel} (G)	70	107

best fit \mathbf{g} and \mathbf{hf} parameters are reported in Table 1 along with the line broadening (LB) used for the simulations for each component. The proportion of the second component increases with oxidation time. (Note: The EPR spectrum at “0 h” of air exposure is the EPR spectrum obtained immediately after particle purification, which involves ~ 20 min of air exposure. This air exposure is enough to result in the emergence of an LSPR. However, at this time point, while there may be free charge carriers, no EPR signal is observed, indicating that the concentration of Cu^{2+} is below the detection limit of the EPR instrument (Figure S1).)

As the ambient exposure time of the NPs increases, there is a change in the relative fractions of the two components present in the EPR spectra (Figure 2). The changing component

fractions suggest an evolution in the population of Cu^{2+} electronic environments in the NP. The relative fraction of component 2 as a function of exposure time is plotted in Figure 3. After ~ 76 h of air exposure, the NPs reach a steady

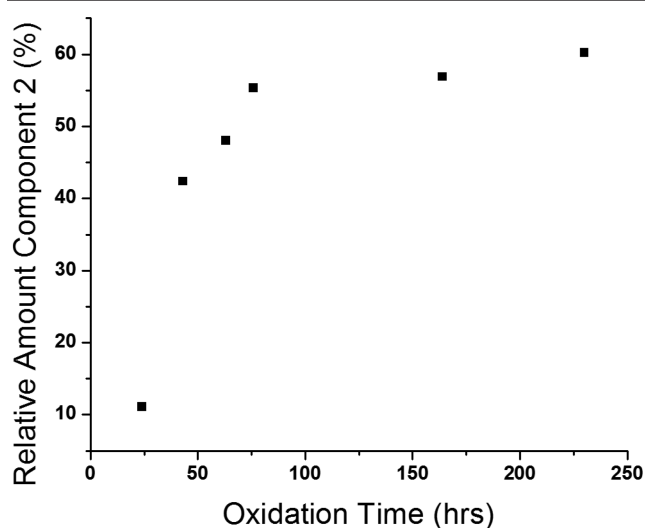


Figure 3. Time evolution of the second electronic environment, which reaches a steady state after ~ 76 h and comprises $\sim 60\%$ of the total Cu^{2+} environments.

state between the two environments, with $\sim 60\%$ of the Cu^{2+} in the second electronic environment. This time scale and the corresponding environment fractions are consistent across multiple synthetic batches of NPs (Figure S2).

While two Cu^{2+} environments are observed in our initial EPR assessment, these Cu^{2+} environments could correspond to four possible families of Cu^{2+} positions: Cu^{2+} coordinating to the OLA capping ligand on the particle surface, Cu^{2+} coordinating to surface or core Se atoms, Cu^{2+} coordinating to O in a copper oxide, or Cu^{2+} being ejected from the NP to form “free” Cu^{2+} coordinated to various ligands (or solvent) in solution (Figure 4).

In addition to monitoring the CW EPR spectra of Cu_{2-x}Se NPs as a function of air exposure over time, corresponding extinction spectra were also obtained at each time point analyzed (Figures S3 and S4; the end-point extinction spectra of the exact particle samples discussed above are shown in Figure 5). The time of air exposure plays an important role in the observed optoelectronic properties of the NPs. As has been previously reported by several groups, including our own, the frequency of the LSPR is dependent on the degree of NP oxidation.^{4,15–17} Our LSPR studies start with NPs that have been oxidized during the washing procedure. (Note that the washing procedure requires the use of ethanol, a known hole scavenger, and therefore the presence of ethanol could influence the LSPR properties of Cu_{2-x}Se .²⁹ However, all particles are dried after the ethanol purification procedure, which removes remaining solvent (Figure S5).)

After the final CW EPR measurement, the extinction spectrum was recorded again. In this spectrum, the LSPR λ_{max} has blue-shifted ~ 70 nm and is coupled with a decrease in the peak width. In addition, the relative intensity of the LSPR increases over the time course of the EPR measurements (230 h), as benchmarked to the band gap transition intensity at ~ 500 nm.

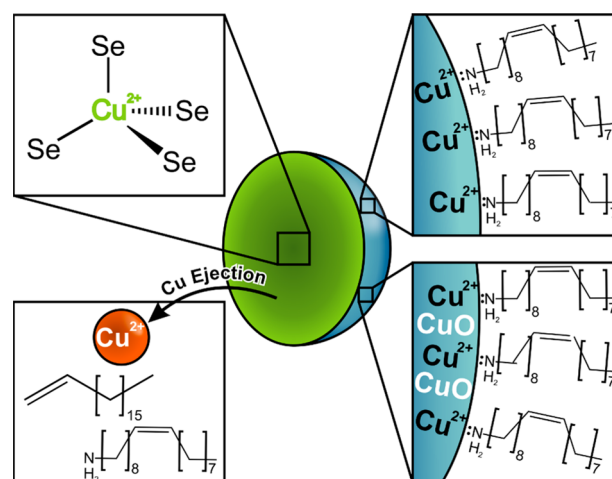


Figure 4. Illustration of the potential Cu^{2+} environments contained in Cu_{2-x}Se NP samples. Starting from the top left and moving clockwise, there is Cu^{2+} coordinated to Se in tetrahedral positions in the antifluorite Cu_{2-x}Se lattice, Cu^{2+} at the surface of the NP coordinating the OLA capping ligand, Cu^{2+} in an oxide layer, or Cu^{2+} ejected from the NP and coordinating to excess OLA capping ligand and/or solvent. Note: Both Se and Cu^{+} environments are omitted for clarity.

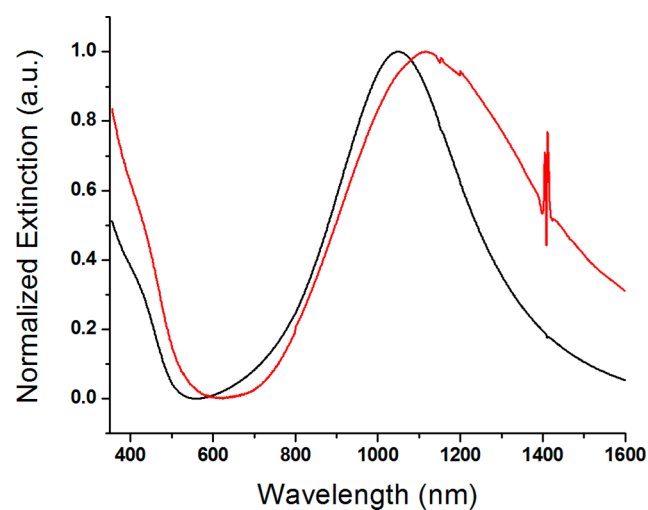


Figure 5. End-point extinction spectra of Cu_{2-x}Se NPs taken immediately after washing (red) and after 230 h of oxidation (black). After oxidation, the λ_{max} shifts 70 nm, the peak width narrows, and the intensity increases relative to the band gap transition near 500 nm.

We solved for the charge carrier density of the tested particles using both these extinction spectra and NMR-based approaches. We used the extinction spectra and the Drude model, which is given as:

$$\omega_{\text{sp}} = \sqrt{\frac{N_{\text{h}}e^2}{(m^*\epsilon_0)(\epsilon_{\infty} + 2\epsilon_{\text{m}})} - \gamma^2}$$

where ω_{sp} is the frequency of the LSPR, N_{h} is the charge carrier density, e is the elementary charge, m^* is the effective mass of the charge carrier, ϵ_0 is the permittivity of free space, ϵ_{∞} is the high frequency dielectric constant of Cu_{2-x}Se , ϵ_{m} is the dielectric constant of the solvent, and γ is the full width at half-maximum (fwhm) of the LSPR.^{6,30} The charge carrier densities obtained for the end-point spectra using this method are 6.45

$\times 10^{21}$ and $7.96 \times 10^{21} \text{ cm}^{-3}$, respectively. However, as noted elsewhere, shifts in λ_{max} may represent a change not only in N_{h} but also in dielectric environment, particle structure, and/or aggregation state, among other variables.^{30–32}

As we have previously reported, the ^{77}Se chemical shift and T_1 values are also indicative of N_{h} for Cu_{2-x}Se NPs.⁴ Upon particle oxidation, the ^{77}Se peak position shifts 44.5 ppm downfield, consistent with increasing N_{h} (Figure S6). Quantification of N_{h} is obtained through measurement of the ^{77}Se T_1 (Figure S7). The T_1 of ^{77}Se in the Cu_{2-x}Se NPs decreases from 2.37 to 2.36 ms between the initial particle oxidation event and 230 h of air exposure. The following relationship is used to calculate N_{h} :

$$N_{\text{h},\text{s}} = \left[\frac{m_{\text{r}}^{*2} N_{\text{h},\text{r}}^{2/3} \left(\frac{T_{1,\text{r}}}{T_{1,\text{s}}} \right)}{m_{\text{s}}^{*2} \left(\frac{T_{1,\text{r}}}{T_{1,\text{s}}} \right)} \right]^{3/2}$$

where N_{h} is the charge carrier density, m^* is the effective mass of the charge carrier, and the subscripts “s” and “r” refer to the values obtained for the sample and reference compound, respectively. Here, bulk Cu_{2-x}Se was used as the reference compound where $N_{\text{h},\text{r}} = 8.0 \times 10^{21} \text{ cm}^{-3}$, $T_{1,\text{r}} = 4.0 \text{ ms}$, and $m_{\text{r}}^* = m_{\text{s}}^* = 0.33m_{\text{e}}$.^{4,33}

Interestingly, the subtle changes in the measured T_1 result in calculation of the same N_{h} ($1.75 \times 10^{22} \text{ cm}^{-3}$) for both the initial and final Cu_{2-x}Se NPs. These results are consistent with theoretical predictions about the sensitivity of T_1 to changes in N_{h} where the sensitivity of T_1 to N_{h} decreases as a function of increasing carrier density (as does the Drude model using the LSPR λ_{max} ; see the Supporting Information for details and supporting calculations).

DISCUSSION

Assigning Cu^{2+} Chemical Environments. Our experiments revealed the presence of two distinct Cu^{2+} environments within oxidized Cu_{2-x}Se NPs. To reiterate, the possible Cu^{2+} environments under consideration are Cu^{2+} coordinating to the OLA ligand on the NP surface, Cu^{2+} coordinating to surface or core Se atoms, Cu^{2+} within an oxide, or ejected Cu^{2+} that has subsequently formed molecular complexes with solvent molecules and/or various ligands in solution (Figure 4). To assign the two observed Cu^{2+} environments, we compare our experimental results to the spectra of known systems.

First, we consider the case of the “free” Cu^{2+} coordinating to ligands available in solution. To study this possibility, we measured the CW EPR spectra of a standard Cu^{2+} control (here, CuCl_2 in water), CuCl (i.e., the Cu^+ precursor used in synthesis) mixed with oleylamine (Cu + OLA) in chloroform, and CuCl mixed with octadecene (Cu + ODE) in chloroform, all subjected to the same heat treatment and washing procedures as outlined in the Cu_{2-x}Se NP synthesis (vide supra). We also investigated the CW EPR spectrum of an additional Cu^{2+} control (CuCl_2 mixed with oleylamine suspended in chloroform *without* heat treatment (i.e., not mimicking synthesis conditions, referred to here as Cu + OLA + no heat)).

The EPR spectra and simulations of each of these mixtures are shown in Figure S9, and their corresponding simulation parameters are given in Table S1. The heat-treated CuCl_2 as well as the Cu + ODE mixtures exhibit different \mathbf{g} and \mathbf{hf} parameters from those measured for either of the two

components of the NPs. Specifically, the g_{\perp} values are larger (~ 0.04) while the A_{\parallel} values are smaller ($\sim 30\text{--}50 \text{ G}$) than those derived for the two components of the NPs. Likewise, the Cu + OLA + no heat mixture has unique \mathbf{g} and \mathbf{hf} tensors that are different from either NP component (Figure S9 and Table S1).

Interestingly, the \mathbf{hf} and \mathbf{g} tensors of the Cu + OLA mixture (the mixture that underwent treatment consistent with synthesis conditions including heat) are similar to those derived for component 1 of the NPs, but the spectrum does not contain evidence of component 2 (Figure 6). SEM of this

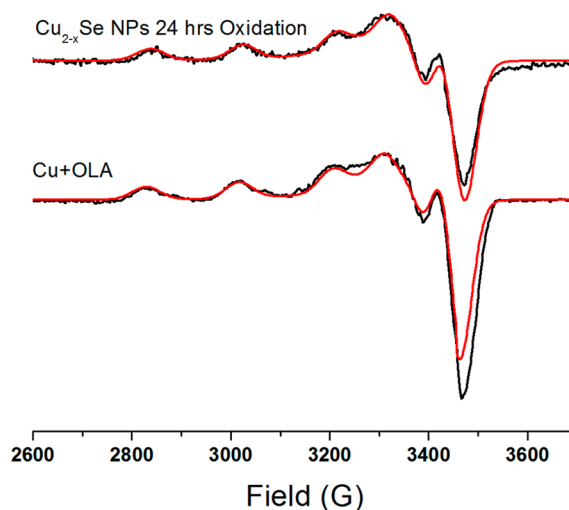


Figure 6. Experimental CW EPR spectra (black) and simulations (red) of Cu_{2-x}Se NPs oxidized for 24 h (top) compared to Cu-OLA coordination complex (bottom) formed via heating. The results indicate component 1 is a surface Cu-OLA environment.

mixture (Figure S10) shows no discernible particles formed upon heating and instead indicates the formation of a Cu-OLA coordination polymer aggregate. Because component 1 from the NPs does not resemble any of the other above controls, including Cu + OLA + no heat, we may deduce that the similarities between component 1 of the NPs and the Cu + OLA mixture indicate that the first Cu^{2+} environment is associated with OLA on the particle surface (i.e., we do not expect OLA- Cu^{2+} interactions occurring on the interior of the particle). Of course, it could also be argued that there is a fraction of Cu-OLA polymer aggregate present in the NP sample. However, no EPR signal was detected from the initial NP sample (Figure S1), and therefore no detectable coordination polymer is present in the NP sample after washing. Taken together, these results support the assignment of one Cu^{2+} environment to surface bound Cu-OLA complexes. These results are in agreement with previous ICP-MS results, which indicate that Cu is not ejected from the NP and is not coordinating to solvent ligands during the oxidation process.⁴

Having initially assigned one electronic environment to Cu-OLA surface sites, we next study whether there is formation of a distinct surface oxide layer. Surface oxide formation is suspected in previous studies of Cu_{2-x}Se NP systems^{15,16,19} and has also been observed in pure Cu NPs (forming Cu@CuO, core@shell morphologies).^{34–38} To investigate whether the second Cu^{2+} environment is due to the formation of a copper oxide layer, we measured the CW EPR spectrum of

Cu@CuO NPs for comparison. Here, Cu NPs were synthesized with OLA as a capping ligand, using a previously reported procedure.^{21,39} TEM, extinction spectra, and XPS characterization of the resulting particles are shown in Figures S11–S13.

In the Cu@CuO NP system, only paramagnetic Cu²⁺ in the oxide layer results in an EPR signal. Simulation of the CW EPR spectrum of Cu@CuO NPs also requires a two-component fit. Comparison of the components for fully oxidized Cu_{2-x}Se NPs and Cu@CuO NPs is shown in Figure 7. The g_{\parallel} and A_{\parallel} values

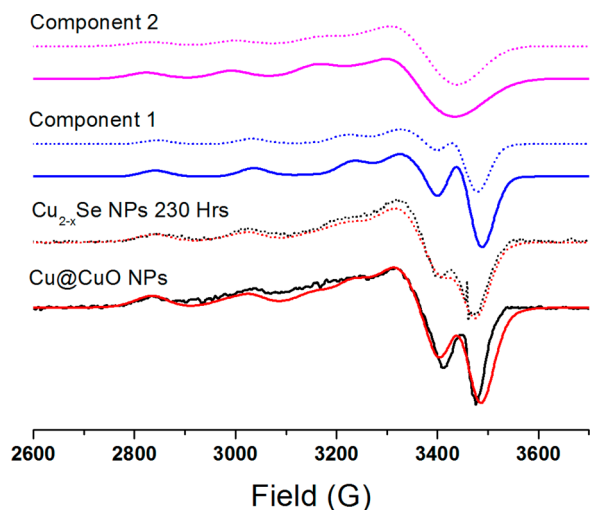


Figure 7. CW EPR spectra (black) and corresponding simulations (red) for Cu@CuO NPs (solid lines) and Cu_{2-x}Se NPs oxidized for 230 h (dotted lines). The spectra have been referenced to the same frequency to highlight to similarities between the g and hf values obtained for component 1 (blue) and component 2 (pink) of the two NP systems. These results indicate that component 2 of the Cu_{2-x}Se NPs is likely a CuO environment.

obtained for Cu@CuO NPs components 1 and 2 agree well with components 1 and 2 of Cu_{2-x}Se NPs, respectively (Table S1), which indicates similar electronic environments between the NP systems. The OLA capping ligand is consistent for both NP systems providing a similar surface Cu–OLA environment for the Cu@CuO and Cu_{2-x}Se NPs, which is already assigned to component 1. Therefore, we assign component 2 of the EPR spectrum from Cu@CuO NPs to CuO. By analogy, these results indicate the formation of CuO on Cu_{2-x}Se NPs as well. Importantly, in both the Cu@CuO NPs and Cu_{2-x}Se NPs, the CuO component shows increased broadening, a decrease in the A_{\parallel} splittings, and an increase in g_{\parallel} compared to the Cu–OLA component. These trends are consistent with decreasing nitrogen and increasing oxygen coordination.⁴⁰

The presence of CuO in the Cu_{2-x}Se NPs was also evaluated using XPS measurements (Figure S15). We observe the emergence of Cu 2p satellite peaks near ~940–945 and ~962 eV, which increase in intensity with increasing oxidation time, similar to results obtained by Prieto et al.¹⁹ The appearance of these peaks is consistent with the XPS spectra of Cu@CuO NPs (Figure S11) and further corroborates the formation of CuO species on the surface of Cu_{2-x}Se NPs.

Unfortunately, the CW EPR spectrum of the Cu@CuO NPs cannot be directly compared to bulk CuO because bulk CuO is antiferromagnetic and will not yield an EPR signal unless annealed at high temperatures.⁴¹ In both the Cu@CuO and Cu_{2-x}Se NPs, the domain size of the CuO must be small

enough that antiferromagnetic behavior is not observable. Indeed, a previous study of the magnetic behavior of CuO NPs clearly demonstrates antiferromagnetic behavior at room temperature in particles with diameters of 6.6 nm, which inadvertently gives an upper limit on the size of the CuO domains we are observing in the Cu_{2-x}Se NPs.⁴²

It is important to note that the second electronic environment observed from the Cu_{2-x}Se NPs may also be a Cu–Se interaction. To evaluate whether the second environment was associated with Cu–Se interactions, we obtained a bulk, powdered sample of Cu₂Se and stored the material in air. After storage, the formation of Cu_{2-x}Se in the sample was discernible in PXRD spectra (Figure S14). The PXRD indicates the presence of both cubic Cu_{2-x}Se and monoclinic Cu₂Se phases. The EPR spectra and corresponding simulation parameters are given in Figure S9 and Table S1. Here, the g ($g_{\parallel} = 2.3780$, $g_{\perp} = 2.0654$) and A ($A_{\parallel} = 150$ G, $A_{\perp} = 1$ G) values are in agreement with Cu(OH)₂ formation and are not representative of either component observed from the Cu_{2-x}Se NPs.⁴³

EPR offers additional methods to investigate and assign Cu²⁺ environments by analyzing next-nearest-neighbor interactions. Here, we use electron spin echo envelope modulation (ESEEM) to study the Cu_{2-x}Se NPs after 230 h of oxidation in deuterated chloroform (Figure 8). Specifically, at X-band,

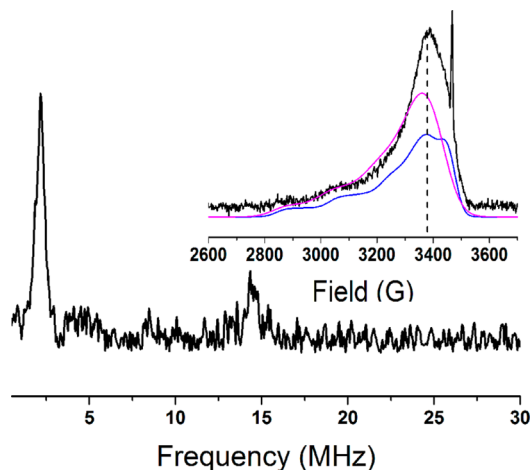


Figure 8. ESEEM spectrum of Cu_{2-x}Se NPs oxidized 230 h suspended in deuterated chloroform. The two peaks correspond to ²D and ¹H frequencies indicating distal coordination of the solvent and ligand to the Cu²⁺ environments. The inset is the echo-detected field swept spectrum. The dashed line corresponds to the field at which the ESEEM was performed (3370 G), which excited 40% component 1 and 60% component 2. The sharp feature at 3466 G corresponds to signal from the quartz sample tube.

the ESEEM experiment probes the hyperfine interaction between the unpaired electron spin of Cu²⁺ and uncoordinated spin active nuclei within 3–8 Å. The frequencies of these hyperfine interactions are reported by the ESEEM experiment and can serve as a fingerprint of the distally coordinated nuclei.⁴⁴ For ¹H and ²D the ESEEM spectra would show peaks at ~14 and ~2 MHz, respectively. For the case of distal ¹⁴N, three characteristic peaks below 3 MHz and a broad peak between 3 and 8 MHz are observed.⁴⁴

The ESEEM spectrum of Cu_{2-x}Se NPs (230 h) suspended in deuterated chloroform (Figure 8) has two peaks at ~2 and ~14 MHz, corresponding to ²D and ¹H, respectively. The

ESEEM was performed at 3370 G (shown in Figure 8, inset), at which field component 1 comprises ~40% of the total signal and component 2 comprises 60%. Thus, we expect to see contributions to the overall ESEEM spectrum from both magnetic environments. The frequency of these peaks indicates that one or both of the Cu^{2+} environments is spatially close to the solvent (^2D and ^1H) and/or the ligand shell (^1H). The lack of distinct ^{14}N ESEEM peaks is consistent with the direct coordination of ^{14}N from OLA to Cu^{2+} . However, surface Cu^{2+} species in close proximity to a Cu–OLA may also produce a ^{14}N ESEEM signal. The absence of any distinct ^{14}N signals indicates the distance between the OLA ^{14}N and the next-nearest Cu^{2+} neighbor must be $>8 \text{ \AA}$ or that the concentration of Cu^{2+} – ^{14}N interactions is below the detection limit of the instrument. These results suggest that the Cu_{2-x}Se NPs have a low ligand density.

Because ^{77}Se is spin-active and has a Larmor frequency of 2.96 MHz which may be reported by ESEEM, we repeated the experiment in nondeuterated solvent (Figure S16) to confirm our assignment of the ~2 MHz peak as deuterium. This ESEEM spectra showed only an ~14 MHz ^1H peak, indicating that the ~2 MHz peak in Figure 8 is due to deuterium. However, due to the low natural abundance of ^{77}Se (7%), we cannot take this data as definitive evidence of the absence of Cu^{2+} – ^{77}Se environments. Taken together, the ESEEM results are consistent with our assignment of component 1 as surface ligand Cu–OLA and component 2 as a CuO environment isolated from OLA ligands.

Impact of Oxidation on the Structure of Cu_{2-x}Se NPs.

Our EPR analysis provides critical insight into the fate of the Cu^{2+} species which has implications for its crystal structure and stoichiometry. Nominally, fully reduced Cu_2Se NPs exhibit a monoclinic or orthorhombic structure. The oxidation of Cu_2Se NPs results in the formation of cubic antiferromagnetic Cu_{2-x}Se .^{4,7,15,19} However, there remains debate about the fate of the Cu^{2+} in Cu_{2-x}Se NPs. In bulk Cu_2Se , this structural transformation is accompanied by the formation of vacancies on the Cu sublattice. At the nanoscale, two scenarios have been previously reported: (I) Cu^{2+} leaves the NP to either form “free” Cu^{2+} species and/or small, discrete (2–5 nm) CuO NPs and/or (II) oxidized Cu^{2+} migrates to the surface of the NP.^{15,17,19}

The released Cu^{2+} ions would give a distinct EPR resonance, akin to that of CuCl_2 or $\text{Cu} + \text{OLA} + \text{no heat}$, which we do not observe in our experiments. On the other hand, the formation of CuO NPs would give rise to similar EPR signatures to what we have observed, assuming the NPs stayed below the domain size of antiferromagnetic CuO (<6–7 nm). To assess the possibility that our samples may contain discrete CuO NPs, we analyzed samples via TEM techniques. Analysis of the resulting micrographs (Figure S17) showed no evidence of 2–5 nm particle formation, and we also did not observe CuO phases in the XRD patterns of any of the tested particles (Figure S18), although the absence of PXRD features is not definitive to exclude the presence of CuO NPs. In our experiments, case I (Cu leaving to form CuO or free Cu) is not supported. Instead, our results indicate that Cu^{2+} either exists as part of a CuO surface layer or may occupy the initial Cu positions within the particle lattice.^{16,19} Taken together with the ESEEM, our results suggest the Cu^{2+} environments are localized at the surface of the NP (case II). Migration of Cu^{2+} to the surface would result in the formation of a crystallographic vacancy as well as a hole charge carrier. The

presence of vacancies is further supported by variable temperature ^{77}Se NMR spectroscopy.

Plotted in Figure 9, there is an increase in the fwhm of the 1 dimensional spectra as sample temperature decreases.

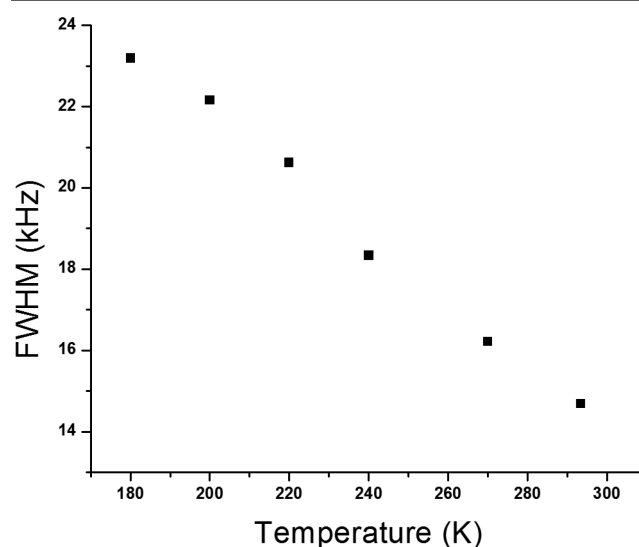


Figure 9. Variable temperature NMR measurements of fwhm of Cu_{2-x}Se NPs. The increase in line width with decreasing temperature corresponds to a decrease in vacancy hopping motion.

Selenium environments in a cubic symmetry will be invariant to temperature fluctuations. However, the formation of vacancies removes the cubic symmetry of the Se environments, resulting in peak broadening from the resultant chemical shift anisotropy (CSA). Vacancy hopping faster than the CSA width will result in an average chemical shift that mirrors the line shape of a cubic crystallographic environment. Upon cooling, the vacancy motion is slowed and results in an observable CSA. Indeed, the low-temperature line shape is fundamentally different than that of the high-temperature (294 K) spectrum (Figure S19). The lack of a clear plateau in the fwhm in the low-temperature regime may suggest vacancy motion is still present at low temperatures. The presence of vacancy motion at low temperature would then indicate low activation energy for vacancy hopping and is consistent with ready migration of Cu^{2+} to the particle surface.

CONCLUSIONS

We report the evolution of Cu^{2+} environments in Cu_{2-x}Se NPs during air-mediated oxidation. The EPR results indicate the presence of two distinct Cu^{2+} environments: one associated with surface bound Cu atoms coordinating to the molecular ligand OLA and the other attributed to the formation of surface-bound CuO.

With the structural characterization presented in this work, there are several research questions that remain and arise. For example, the formation of CuO layer may directly impact the observed LSPR by changing the dielectric functions of the nanoparticle and the medium. In addition, the CuO layer may promote activation of charge carriers leading to non-negligible changes in N_h that supersede changes in the NP stoichiometry from oxidation.^{31,45} Finally, the observation of vacancies and vacancy hopping motion may provide insight into the room temperature phase changes observed upon NP oxidation.

■ ASSOCIATED CONTENT

S Supporting Information

The Supporting Information is available free of charge on the ACS Publications website at DOI: [10.1021/acs.chemmater.8b03967](https://doi.org/10.1021/acs.chemmater.8b03967).

Additional EPR, PXRD, extinction spectroscopy, NMR, XPS, SEM, and TEM characterization of the Cu_{2-x}Se and Cu@CuO NPs (PDF)

■ AUTHOR INFORMATION

Corresponding Authors

*E-mail: jem210@pitt.edu (J.E.M.).

*E-mail: sksaxena@pitt.edu (S.S.).

ORCID 

Sunil Saxena: 0000-0001-9098-6114

Jill E. Millstone: 0000-0002-9499-5744

Present Address

D.C.K.: Los Alamos National Laboratory, Los Alamos, NM.

Notes

The authors declare no competing financial interest.

■ ACKNOWLEDGMENTS

This work was supported by the Defense Threat Reduction Agency (Grant HDTRA1-16-1-0044), the Research Corporation for Science Advancement, and the National Science Foundation (NSF MCB-1613007). The EPR spectrometer was supported by the National Science Foundation (NSF MRI-1725678). X.Y.G. thanks the Pittsburgh Quantum Institute for a Graduate Student Fellowship.

■ REFERENCES

- (1) Macdonald, J. E.; Kelly, J. A.; Veinot, J. G. C. Iron/Iron Oxide Nanoparticle Sequestration of Catalytic Metal Impurities from Aqueous Media and Organic Reaction Products. *Langmuir* **2007**, *23*, 9543–9545.
- (2) Shi, G.; Shen, J. New Synthesis Method for Nickel Phosphide Nanoparticles: Solid Phase Reaction of Nickel Cations with Hypophosphites. *J. Mater. Chem.* **2009**, *19*, 2295–2297.
- (3) Das, D.; Pal, M.; Di Bartolomeo, E.; Traversa, E.; Chakravorty, D. Synthesis of Nanocrystalline Nickel Oxide by Controlled Oxidation of Nickel Nanoparticles and Their Humidity Sensing Properties. *J. Appl. Phys.* **2000**, *88*, 6856–6860.
- (4) Marbella, L. E.; Gan, X. Y.; Kaseman, D. C.; Millstone, J. E. Correlating Carrier Density and Emergent Plasmonic Features in Cu_{2-x}Se Nanoparticles. *Nano Lett.* **2017**, *17*, 2414–2419.
- (5) Agrawal, A.; Cho, S. H.; Zandi, O.; Ghosh, S.; Johns, R. W.; Milliron, D. J. Localized Surface Plasmon Resonance in Semiconductor Nanocrystals. *Chem. Rev.* **2018**, *118*, 3121–3207.
- (6) Luther, J. M.; Jain, P. K.; Ewers, T.; Alivisatos, A. P. Localized Surface Plasmon Resonances Arising from Free Carriers in Doped Quantum Dots. *Nat. Mater.* **2011**, *10*, 361–366.
- (7) Kriegel, I.; Scotognella, F.; Manna, L. Plasmonic Doped Semiconductor Nanocrystals: Properties, Fabrication, Applications and Perspectives. *Phys. Rep.* **2017**, *674*, 1–52.
- (8) Huang, X.; Zhang, W.; Guan, G.; Song, G.; Zou, R.; Hu, J. Design and Functionalization of the NIR-Responsive Photothermal Semiconductor Nanomaterials for Cancer Theranostics. *Acc. Chem. Res.* **2017**, *50*, 2529–2538.
- (9) Sun, S.; Li, P.; Liang, S.; Yang, Z. Diversified Copper Sulfide (Cu_{2-x}S) Micro-/Nanostructures: A Comprehensive Review on Synthesis, Modifications and Applications. *Nanoscale* **2017**, *9*, 11357–11404.
- (10) Yan, C.; Tian, Q.; Yang, S. Recent Advances in the Rational Design of Copper Chalcogenide to Enhance the Photothermal

Conversion Efficiency for the Photothermal Ablation of Cancer Cells. *RSC Adv.* **2017**, *7*, 37887–37897.

(11) Liu, Y.; Liu, M.; Swihart, M. T. Plasmonic Copper Sulfide-Based Materials: A Brief Introduction to Their Synthesis, Doping, Alloying, and Applications. *J. Phys. Chem. C* **2017**, *121*, 13435–13447.

(12) Hessel, C. M.; Pattani, V. P.; Rasch, M.; Panthani, M. G.; Koo, B.; Tunnell, J. W.; Korgel, B. A. Copper Selenide Nanocrystals for Photothermal Therapy. *Nano Lett.* **2011**, *11*, 2560–2566.

(13) Li, W.; Zamani, R.; Rivera Gil, P.; Pelaz, B.; Ibáñez, M.; Cadavid, D.; Shavel, A.; Alvarez-Puebla, R. A.; Parak, W. J.; Arbiol, J.; Cabot, A. CuTe Nanocrystals: Shape and Size Control, Plasmonic Properties, and Use as SERS Probes and Photothermal Agents. *J. Am. Chem. Soc.* **2013**, *135*, 7098–7101.

(14) Hsu, S.-W.; On, K.; Tao, A. R. Localized Surface Plasmon Resonances of Anisotropic Semiconductor Nanocrystals. *J. Am. Chem. Soc.* **2011**, *133*, 19072–19075.

(15) Dorfs, D.; Härtling, T.; Miszta, K.; Bigall, N. C.; Kim, M. R.; Genovese, A.; Falqui, A.; Povia, M.; Manna, L. Reversible Tunability of the Near-Infrared Valence Band Plasmon Resonance in Cu_{2-x}Se Nanocrystals. *J. Am. Chem. Soc.* **2011**, *133*, 11175–11180.

(16) Kriegel, I.; Jiang, C.; Rodríguez-Fernández, J.; Schaller, R. D.; Talapin, D. V.; da Como, E.; Feldmann, J. Tuning the Excitonic and Plasmonic Properties of Copper Chalcogenide Nanocrystals. *J. Am. Chem. Soc.* **2012**, *134*, 1583–1590.

(17) Wolf, A.; Kodanek, T.; Dorfs, D. Tuning the LSPR in Copper Chalcogenide Nanoparticles by Cation Intercalation, Cation Exchange and Metal Growth. *Nanoscale* **2015**, *7*, 19519–19527.

(18) Hartstein, K. H.; Brozek, C. K.; Hinterding, S. O. M.; Gamelin, D. R. Copper-Coupled Electron Transfer in Colloidal Plasmonic Copper-Sulfide Nanocrystals Probed by in Situ Spectroelectrochemistry. *J. Am. Chem. Soc.* **2018**, *140*, 3434–3442.

(19) Riha, S. C.; Johnson, D. C.; Prieto, A. L. Cu_2Se Nanoparticles with Tunable Electronic Properties Due to a Controlled Solid-State Phase Transition Driven by Copper Oxidation and Cationic Conduction. *J. Am. Chem. Soc.* **2011**, *133*, 1383–1390.

(20) Deka, S.; Genovese, A.; Zhang, Y.; Miszta, K.; Bertoni, G.; Krahn, R.; Giannini, C.; Manna, L. Phosphine-Free Synthesis of p-Type Copper(I) Selenide Nanocrystals in Hot Coordinating Solvents. *J. Am. Chem. Soc.* **2010**, *132*, 8912–8914.

(21) Shi, M.; Kwon, H. S.; Peng, Z.; Elder, A.; Yang, H. Effects of Surface Chemistry on the Generation of Reactive Oxygen Species by Copper Nanoparticles. *ACS Nano* **2012**, *6*, 2157–2164.

(22) Stoll, S.; Schweiger, A. EasySpin, a Comprehensive Software Package for Spectral Simulation and Analysis in EPR. *J. Magn. Reson.* **2006**, *178*, 42–55.

(23) Gemperle, C.; Aebli, G.; Schweiger, A.; Ernst, R. R. Phase Cycling in Pulse EPR. *J. Magn. Reson.* **1990**, *88*, 241–256.

(24) Fauth, J. M.; Schweiger, A.; Braunschweiler, L.; Forrer, J.; Ernst, R. R. Elimination of Unwanted Echoes and Reduction of Dead Time in Three-Pulse Electron Spin-Echo Spectroscopy. *J. Magn. Reson.* **1986**, *66*, 74–85.

(25) Ammann, C.; Meier, P.; Merbach, A. A Simple Multinuclear NMR Thermometer. *J. Magn. Reson.* **1982**, *46*, 319–321.

(26) Collins, M. J.; Ratcliffe, C. I.; Ripmeester, J. A. CP/MAS ^{77}Se NMR in Solids. Chemical Shift Tensors and Isotropic Shifts. *J. Magn. Reson.* **1986**, *68*, 172–179.

(27) Kivelson, D.; Neiman, R. ESR Studies on the Bonding in Copper Complexes. *J. Chem. Phys.* **1961**, *35*, 149–155.

(28) Delabie, A.; Pierloot, K.; Groothaert, M. H.; Schoonheydt, R. A.; Vanquickenborne, L. G. The Coordination of Cu(II) in Zeolites – Structure and Spectroscopic Properties. *Eur. J. Inorg. Chem.* **2002**, *2002*, 515–530.

(29) Schimpf, A. M.; Knowles, K. E.; Carroll, G. M.; Gamelin, D. R. Electronic Doping and Redox-Potential Tuning in Colloidal Semiconductor Nanocrystals. *Acc. Chem. Res.* **2015**, *48*, 1929–1937.

(30) Mendelsberg, R. J.; Garcia, G.; Li, H.; Manna, L.; Milliron, D. J. Understanding the Plasmon Resonance in Ensembles of Degenerately Doped Semiconductor Nanocrystals. *J. Phys. Chem. C* **2012**, *116*, 12226–12231.

(31) Crockett, B. M.; Jansons, A. W.; Koskela, K. M.; Johnson, D. W.; Hutchison, J. E. Radial Dopant Placement for Tuning Plasmonic Properties in Metal Oxide Nanocrystals. *ACS Nano* **2017**, *11*, 7719–7728.

(32) Agrawal, A.; Johns, R. W.; Milliron, D. J. Control of Localized Surface Plasmon Resonances in Metal Oxide Nanocrystals. *Annu. Rev. Mater. Res.* **2017**, *47*, 1–31.

(33) Mansour, B. A.; Demian, S. E.; Zayed, H. A. Determination of the Effective Mass for Highly Degenerate Copper Selenide from Reflectivity Measurements. *J. Mater. Sci.: Mater. Electron.* **1992**, *3*, 249–252.

(34) Curtis, A. C.; Duff, D. G.; Edwards, P. P.; Jefferson, D. A.; Johnson, B. F. G.; Kirkland, A. I.; Wallace, A. S. Preparation and Structural Characterization of An Unprotected Copper Sol. *J. Phys. Chem.* **1988**, *92*, 2270–2275.

(35) Yanase, A.; Komiyama, H. In situ Observation of Oxidation and Reduction of Small Supported Copper Particles using Optical Absorption and X-ray Diffraction. *Surf. Sci.* **1991**, *248*, 11–19.

(36) van Wijk, R.; Görts, P. C.; Mens, A. J. M.; Gijzeman, O. L. J.; Habraken, F. H. P. M.; Geus, J. W. XPS/NRA Investigations of Particle Size Effects during the Oxidation of Cu Particles Supported on Oxidised Si (100). *Appl. Surf. Sci.* **1995**, *90*, 261–269.

(37) Hambrock, J.; Becker, R.; Birkner, A.; Weiß, Fischer, R. A. A Non-Aqueous Organometallic Route to Highly Monodispersed Copper Nanoparticles Using [Cu(OCH(Me)CH₂NMe₂)₂]. *Chem. Commun.* **2002**, *0*, 68–69.

(38) Wu, S.-H.; Chen, D.-H. Synthesis of High-Concentration Cu Nanoparticles in Aqueous CTAB Solutions. *J. Colloid Interface Sci.* **2004**, *273*, 165–169.

(39) Uk Son, S.; Kyu Park, I.; Park, J.; Hyeon, T. Synthesis of Cu₂O Coated Cu Nanoparticles and Their Successful Applications to Ullmann-Type Amination Coupling Reactions of Aryl Chlorides. *Chem. Commun.* **2004**, *0*, 778–779.

(40) Peisach, J.; Blumberg, W. E. Structural Implications Derived from the Analysis of Electron Paramagnetic Resonance Spectra of Natural and Artificial Copper Proteins. *Arch. Biochem. Biophys.* **1974**, *165*, 691–708.

(41) Singh, R. J.; Punnoose, A.; Mathew, J.; Maurya, B. P.; Umar, M.; Haque, M. I. S = 1 and S = 2 EPR Signals in Modified CuO and BaCuO₂. *Phys. Rev. B: Condens. Matter Mater. Phys.* **1994**, *49*, 1346–1349.

(42) Punnoose, A.; Magnone, H.; Seehra, M. S.; Bonevich, J. Bulk to Nanoscale Magnetism and Exchange Bias in CuO Nanoparticles. *Phys. Rev. B: Condens. Matter Mater. Phys.* **2001**, *64*, 174420–174427.

(43) Würz, R.; Meeder, A.; Fuertes Marrón, D.; Schedel-Niedrig, T.; Knop-Gericke, A.; Lips, K. Native Oxidation of CuGaSe₂ Crystals and Thin Films Studied by Electron Paramagnetic Resonance and Photoelectron Spectroscopy. *Phys. Rev. B: Condens. Matter Mater. Phys.* **2004**, *70*, 205321–205330.

(44) Dikanov, S. A.; Tsvetkov, Y. *Electron Spin Echo Envelope Modulation (ESEEM) Spectroscopy*; CRC Press: 1992.

(45) Lounis, S. D.; Runnerstrom, E. L.; Bergerud, A.; Nordlund, D.; Milliron, D. J. Influence of Dopant Distribution on the Plasmonic Properties of Indium Tin Oxide Nanocrystals. *J. Am. Chem. Soc.* **2014**, *136*, 7110–7116.